



**HAL**  
open science

# Structure, Morphology, and Photoelectric Performances of Te-Sb(2)Se(3)Thin Film Prepared via Magnetron Sputtering

Donglou Ren, Xue Luo, Shuo Chen, Zhuanghao Zheng, Michel Cathelinaud, Guang-Xing Liang, Hongli Ma, Xvsheng Qiao, Xianping Fan, Xianghua Zhang

► **To cite this version:**

Donglou Ren, Xue Luo, Shuo Chen, Zhuanghao Zheng, Michel Cathelinaud, et al.. Structure, Morphology, and Photoelectric Performances of Te-Sb(2)Se(3)Thin Film Prepared via Magnetron Sputtering. *Nanomaterials*, 2020, 10 (7), pp.1358. 10.3390/nano10071358 . hal-02928611

**HAL Id: hal-02928611**

**<https://hal.science/hal-02928611>**

Submitted on 2 Sep 2020

**HAL** is a multi-disciplinary open access archive for the deposit and dissemination of scientific research documents, whether they are published or not. The documents may come from teaching and research institutions in France or abroad, or from public or private research centers.

L'archive ouverte pluridisciplinaire **HAL**, est destinée au dépôt et à la diffusion de documents scientifiques de niveau recherche, publiés ou non, émanant des établissements d'enseignement et de recherche français ou étrangers, des laboratoires publics ou privés.



Distributed under a Creative Commons Attribution 4.0 International License



Article

# Structure, Morphology, and Photoelectric Performances of Te-Sb<sub>2</sub>Se<sub>3</sub> Thin Film Prepared via Magnetron Sputtering

Donglou Ren <sup>1</sup>, Xue Luo <sup>1,2</sup>, Shuo Chen <sup>3</sup>, Zhuanghao Zheng <sup>3</sup>, Michel Cathelinaud <sup>1</sup>, Guangxing Liang <sup>3</sup>, Hongli Ma <sup>1</sup>, Xvsheng Qiao <sup>2</sup>, Xianping Fan <sup>2</sup> and Xianghua Zhang <sup>1,\*</sup>

<sup>1</sup> ISCR (Institut des Sciences Chimiques de Rennes)-CNRS, UMR 6226, Univ. Rennes, F-35000 Rennes, France; rendonglou15@mailsucas.edu.cn (D.R.); xue.luo@univ-rennes1.fr (X.L.); michel.cathelinaud@univ-rennes1.fr (M.C.); hongli.ma@univ-rennes1.fr (H.M.)

<sup>2</sup> State Key Laboratory of Silicon Materials & School of Materials Science and Engineering, Zhejiang University, Hangzhou 310027, China; qiaoxus@zju.edu.cn (X.Q.); fanxp@zju.edu.cn (X.F.)

<sup>3</sup> Shenzhen Key Laboratory of Advanced Thin Films and Applications, College of Physics and Optoelectronic Engineering, Shenzhen University, Shenzhen 518060, China; chensh@szu.edu.cn (S.C.); zhengzh@szu.edu.cn (Z.Z.); lgx@szu.edu.cn (G.L.)

\* Correspondence: xiang-hua.zhang@univ-rennes1.fr; Tel.: +33-02-2323-6937

Received: 22 June 2020; Accepted: 9 July 2020; Published: 11 July 2020



**Abstract:** Antimony selenide (Sb<sub>2</sub>Se<sub>3</sub>) has been widely investigated as a promising absorber material for photovoltaic devices. However, low open-circuit voltage ( $V_{oc}$ ) limits the power conversion efficiency (PCE) of Sb<sub>2</sub>Se<sub>3</sub>-based cells, largely due to the low-charge carrier density. Herein, high-quality n-type (Tellurium) Te-doped Sb<sub>2</sub>Se<sub>3</sub> thin films were successfully prepared using a homemade target via magnetron sputtering. The Te atoms were expected to be inserted in the spacing of (Sb<sub>4</sub>Se<sub>6</sub>)<sub>n</sub> ribbons based on increased lattice parameters in this study. Moreover, the thin film was found to possess a narrow and direct band gap of approximately 1.27 eV, appropriate for harvesting the solar energy. It was found that the photoelectric performance is related to not only the quality of films but also the preferred growth orientation. The Te-Sb<sub>2</sub>Se<sub>3</sub> film annealed at 325 °C showed a maximum photocurrent density of 1.91 mA/cm<sup>2</sup> with a light intensity of 10.5 mW/cm<sup>2</sup> at a bias of 1.4 V. The fast response and recovery speed confirms the great potential of these films as excellent photodetectors.

**Keywords:** Te-Sb<sub>2</sub>Se<sub>3</sub> thin film; magnetron sputtering; structure; photoelectric performances

## 1. Introduction

The current most commercialized thin-film solar cells are copper indium gallium selenide (CIGS) and cadmium telluride (CdTe). Their market share is continuously reducing, mainly due to the scarcity of indium and gallium and the toxicity of cadmium [1,2]. In addition, the complex composition of CIGS is an issue for industrial production. To overcome these problems, many researchers have explored other earth-abundant and nontoxic absorber materials that consist of ribbons, for instance, antimony sulfide (Sb<sub>2</sub>S<sub>3</sub>) [3,4] and antimony selenide (Sb<sub>2</sub>Se<sub>3</sub>) [5–7]. The ribbons are held together by weak van der Waals forces. Once they are parallel to the grain boundary plane, the device performance can be significantly enhanced by eliminating dangling bonds at the grain boundary. Notably, the power conversion efficiency (PCE) of the Sb<sub>2</sub>Se<sub>3</sub> solar cells has had a very rapid evolution within only 7 years, reaching 9.2% in 2019 based on the core-shell nanorod configuration [8]. This is ascribed to a series of excellent properties of this binary material, including a narrow band gap (1.1–1.3 eV), high absorption coefficient ( $>10^5$  cm<sup>-1</sup>) and fast carrier transport along the [001] orientation [5,8–11].

Moreover, the simple composition and the only stable phase in this binary system minimize the risk of impurity phase during thin film preparation.

At present, the PCE of  $\text{Sb}_2\text{Se}_3$  based solar cells is still limited by many poor characteristics such as its low-charge carrier density ( $\sim 10^{13} \text{ cm}^{-3}$ ) and high concentration of intrinsic point defects (vacancies and antisite defects) [10,12]. Thus far, some efficient ways to reduce the intrinsic point defects and prolong the minority carrier lifetimes in thin films are post-selenization [13], in-situ selenium compensation [14], and the use of vapor transport deposition [15]. It is well known that doping is an efficient approach to adjust the defects of semiconductors, which has been widely utilized in the semiconductor industry [16]. However, few studies have been carried out on doped  $\text{Sb}_2\text{Se}_3$  thin films, and the development of appropriate doping for broadening the applications of this promising material is crucial. Since the notable PCE of 2.26% realized in 2014 [17], many methods of thin film preparation have been proposed [5,8,15,17–19]. Among these approaches, magnetron sputtering can realize high-quality thin film under a full-vacuum deposition condition [13,20,21], and the record PCE of 6.84% was reported by Liang et al in 2020 [22].

This work is on the preparation and characterization of  $\text{Te-Sb}_2\text{Se}_3$  thin films prepared by using the sputtering method. We selected the element Te as a doping atom for different reasons. Firstly, our objective was to obtain a n-type semiconductor and Te has four valence electrons, one more than Sb. Secondly, it is known that Te can minimize defect formation in  $\text{Sb}_2\text{Se}_3$  films [23], which may be correlated with its smaller atomic radius (1.43 Å) [24] in comparison with the gap of  $(\text{Sb}_4\text{Se}_6)_n$  ribbons ( $\sim 3.5$  Å) [25]. The structure, morphology, and photoelectric performances of these thin films were systematically investigated.

## 2. Materials and Methods

High purity elements of antimony (Sb, 99.999%, Umicore), selenium (Se, 99.999%, Umicore), and Tellurium (Te, 99.999%, Umicore) were utilized as raw materials.

### 2.1. Preparation of the $\text{Te-Sb}_2\text{Se}_3$ Target

The  $\text{Te-Sb}_2\text{Se}_3$  target with the chemical composition of  $\text{Sb}_2(\text{Se}_{0.97}\text{Te}_{0.03})_3$  was prepared using a highly reproducible melting method at a high temperature. This composition has previously been optimized in a relationship in terms of its photoelectric properties. At first, a 70-g mixture was weighted in a glovebox under argon according to the chemical composition. Then, the mixture was loaded into a fully cleaned silica tube with an internal diameter of 50 mm. In order to eliminate all volatile substances in the mixture, the tube was evacuated and sealed until a vacuum of about  $10^{-5}$  mbar was reached. Subsequently, the tube was placed in a rocking furnace and heated to 810 °C with a ramp rate of 1.2 °C/min. The mixture was continuously rocked at 810 °C for 10 h, after which the furnace was kept vertical for the crystallization of melt at a cooling rate of 1.2 °C/min. After cooling down to room temperature, the as-prepared specimen was carefully taken out of the silica tube and finely polished into a magnetron sputtering target with a thickness of around 6 mm and a diameter of 50 mm.

### 2.2. Deposition of the $\text{Te-Sb}_2\text{Se}_3$ Thin Films

The  $\text{Te-Sb}_2\text{Se}_3$  thin films were deposited by using a homemade target and a magnetron sputtering system (Plassys MP600S) equipped with an in-line optical monitoring system to measure the reflectance at a certain wavelength and the film thickness in real time. In addition, it can detect the crystallization process, which changes the reflection of the film. More detailed descriptions can be found in our previous works [26,27]. Indium tin oxide (ITO)-coated glasses ( $2.5 \times 2.5 \text{ cm}^2$ ) with a sheet resistance of 30 Ω were used as substrates and consecutively cleaned using detergent, acetone, ethanol, and deionized water for 15 min each. The sputtering chamber was evacuated to a pressure below  $2 \times 10^{-7}$  mbar before deposition. High-purity (99.99%) Ar gas with a mass flow rate of 30 sccm was used for depositing the thin films. The radio frequency (RF) sputtering power was kept at 12 W, and the working pressure was set at 0.04 mbar. Before deposition, the homemade target was pre-sputtered for 10 min to remove the

contaminants from the surface. Afterwards, the thin films were deposited on unheated substrates that were continuously rotated during preparation. All thin films had a thickness of 350 nm, which was measured using the in-situ optical monitoring system and confirmed by observation under electronic microscope. Following that, the thin films were annealed in the range of 325–400 °C under a pressure of 0.1 mbar with 40 sccm flow of Ar for 90 min to induce crystallization. The temperature was monitored utilizing a thermocouple enclosed in the chamber.

### 2.3. Characterization

X-ray diffraction (XRD) with Cu K $\alpha$  radiation was performed to analyze the crystalline structure on a PANalytical X-ray diffractometer in the range of 10–60° under 40 kV and 40 mA. The morphologies were observed by using a thermal field-emission scanning electron microscope (SEM, JEOL JSM-7100 F) equipped with an energy dispersive spectrometer (EDS). The optical properties of the thin films were characterized utilizing a PerkinElmer LAMBDA 1050 UV/Vis/NIR spectrophotometer with dual beam and a monochromator. The transmission and reflection measurements were performed at ambient temperature in a wavelength range of 500 to 1500 nm. The conductivity type of the thin films was determined via a Semilab PN tester PN-100. To evaluate the photoelectric performances of the thin films, photo-electro-chemical (PEC) measurements were carried out using a conventional three-electrode system in 0.5 M LiClO<sub>4</sub> solution, where the thin films, a Pt-wire, and an Ag/AgCl electrode were used as the working, counter, and reference electrodes, respectively. A white light tungsten halogen lamp was used as a light source with a light intensity of 10.5 mW/cm<sup>2</sup>, and a detailed description can be found in our previous works [16,28].

## 3. Results and Discussion

### 3.1. Target Characterization

Figure 1a shows the XRD pattern of the Te-Sb<sub>2</sub>Se<sub>3</sub> target prepared by a melting method at a high temperature in vacuum. As observed, all diffraction peaks matched well with the orthorhombic phase of Sb<sub>2</sub>Se<sub>3</sub> (JCPDS standard card 15-0861) without any noticeable impurities. The target exhibited a preferential crystallographic orientation of [230], largely due to the surface energy of some crystal planes during crystallization from liquid [29]. It was also observed that the polished target possessed a flat surface without cracks and porosity (Figure 1b), suggesting that the preparation method could completely meet the target demand of magnetron sputtering. In comparison with the commonly used spark plasma sintering method [30], the melting method could facilitate mass transport and thus improve the uniformity of the composition [31–33]. In addition, crystallization from a melt is generally exempt from porosity. Moreover, the distribution of elements was uniform, as evidenced by EDS elemental mapping, indicating that the Te element was well doped into the Sb<sub>2</sub>Se<sub>3</sub> lattice. We prepared and characterized three targets and obtained the same results, confirming the repeatability of experiments. Meanwhile, the average composition of these targets is shown in Table 1. The atomic percentages of Sb, Se, and Te were 39.78 ± 0.28, 58.2 ± 0.17, and 2.02 ± 0.03at.%, respectively.

**Table 1.** The energy dispersive spectroscopy (EDS) results of the Te-Sb<sub>2</sub>Se<sub>3</sub> targets prepared by the melting method in a vacuum (average composition).

Element	Sb	Se	Te
Atomic percent (at.%)	39.78 ± 0.28	58.2 ± 0.17	2.02 ± 0.03

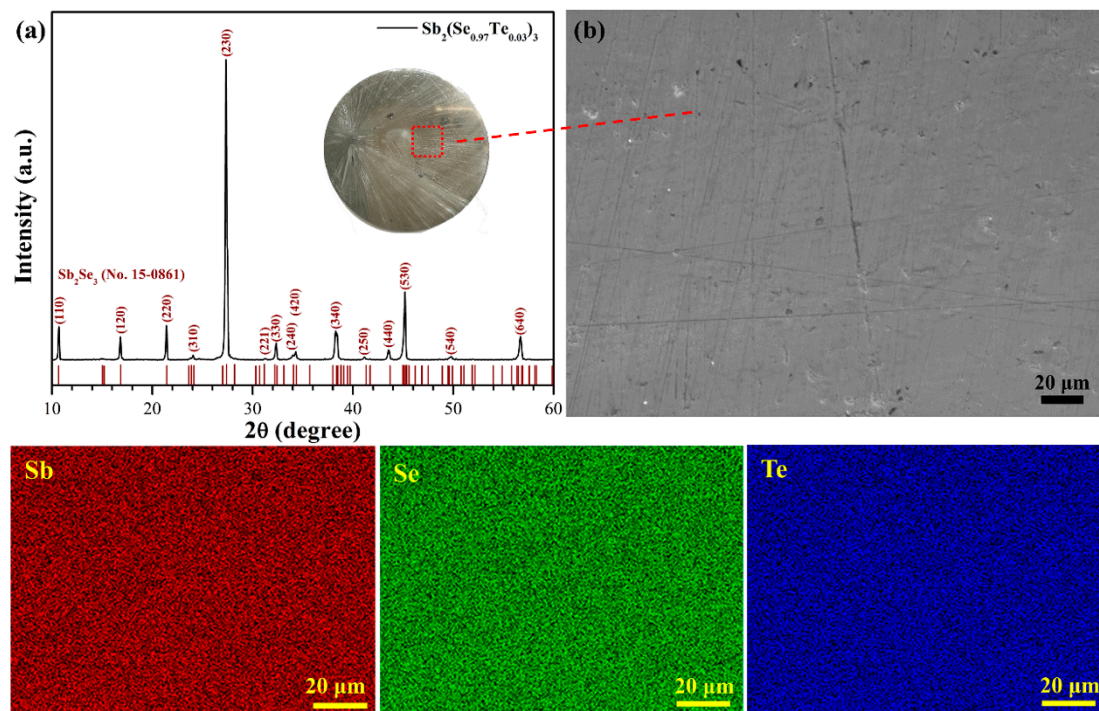


**Figure 1.** (a) The X-ray diffraction (XRD) pattern of the Te-Sb<sub>2</sub>Se<sub>3</sub> target prepared by the melting method. The inset is the surface morphology. (b) Scanning electron microscope (SEM) image and energy dispersive spectroscopy (EDS) elemental mapping of Sb, Se, and Te.

### 3.2. Characterization on the Structure of Te-Sb<sub>2</sub>Se<sub>3</sub> Thin Films

The XRD patterns of the as-deposited and annealed Te-Sb<sub>2</sub>Se<sub>3</sub> thin films with different temperatures are presented in Figure 2a. For the as-deposited thin film, no crystalline diffraction peaks were detected, except for some peaks that originated from the ITO substrate, indicating the amorphous characteristic of the thin films deposited on an unheated substrate. Subsequently, the thin film was annealed in the range of 325–400 °C under Ar atmosphere with an interval of 25 °C. It is obvious that the emerging peaks are in good agreement with the orthorhombic Sb<sub>2</sub>Se<sub>3</sub> (JCPDS standard card 15-0861). At the same time, the sharp diffraction peaks also indicate the highly crystalline nature of these annealed thin films. Most importantly, no impurity phases in any of the XRD patterns revealed that Te element was successfully doped into the lattice of Sb<sub>2</sub>Se<sub>3</sub>. To further confirm the successful doping behavior, we prepared pure Sb<sub>2</sub>Se<sub>3</sub> thin film using the same deposition condition as a reference sample. As observed, the diffraction peak (230) slightly shifted toward a lower angle with Te doping (Figure 2b), which was due to an increase in the interplanar spacing according to Bragg's equation. On the basis of a previous report [23] and by considering its electronic structure, Te cannot substitute for Se atoms in the Sb<sub>2</sub>Se<sub>3</sub> lattice. Consequently, this observation implies that Te atoms are largely doped into the spacing of (Sb<sub>4</sub>Se<sub>6</sub>)<sub>n</sub> ribbons (~3.5 Å) [25]. In addition, it is noteworthy that the intensity of (211) and (221) diffraction peaks first increased and then decreased, accompanied by the reverse trend for the (120) and (020) peaks. The thin film annealed at 350 °C had the highest intensity of (211) and (221) peaks as compared to other crystalline films. Generally, the crystallinity improved with an increasing annealing temperature. However, if the temperature was too high, e.g., 400 °C, the intensity of diffraction peaks showed a slight decrease, which is attributed to the deterioration of the films due to quite high vapor pressure of Sb<sub>2</sub>Se<sub>3</sub> at this temperature [5].

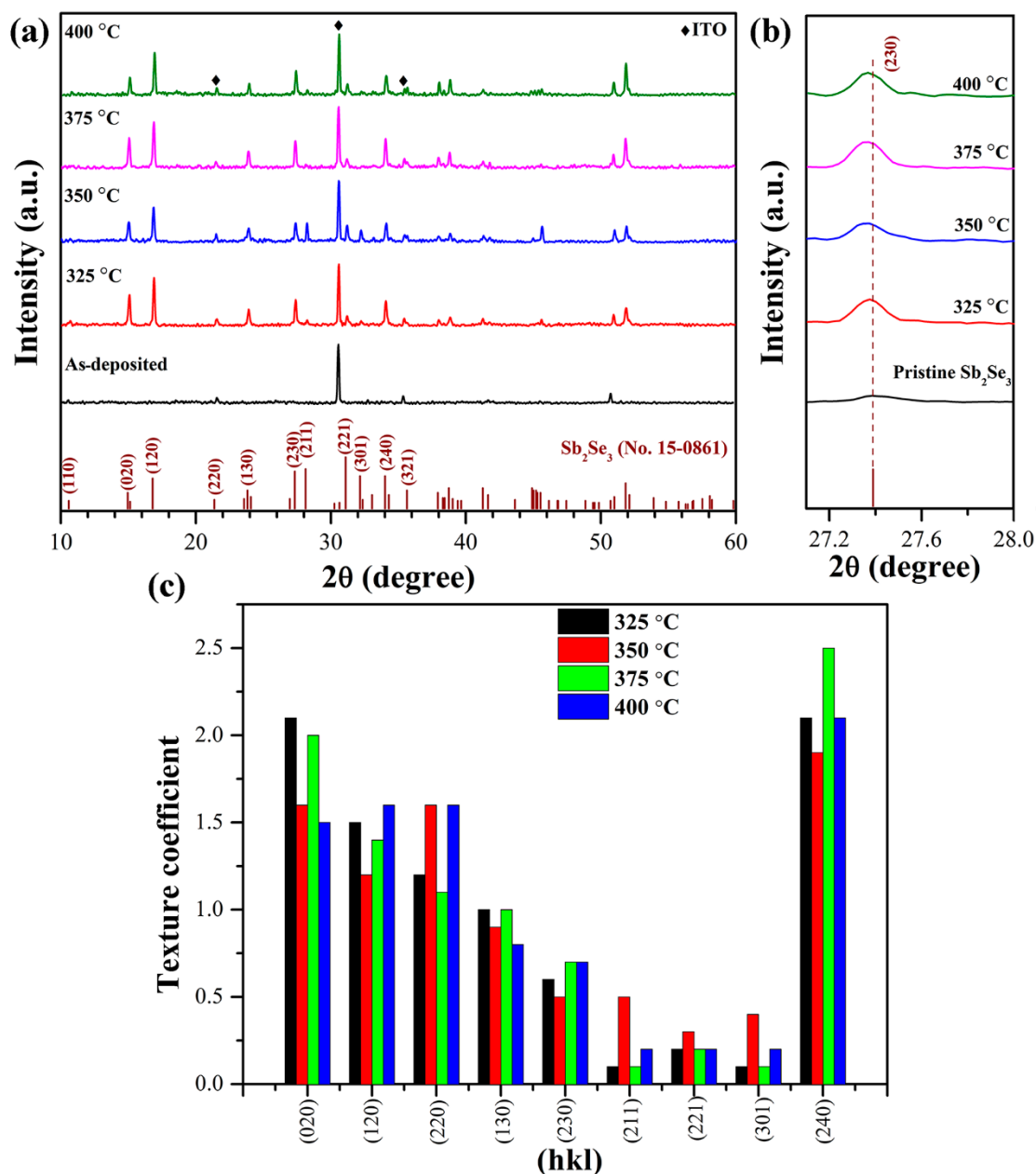


**Figure 2.** (a) XRD patterns of Te-Sb<sub>2</sub>Se<sub>3</sub> thin films on indium tin oxide (ITO) with different annealing temperatures. (b) Shift of (230) peak of crystalline Te-Sb<sub>2</sub>Se<sub>3</sub> thin films as shown in XRD patterns compared with pristine Sb<sub>2</sub>Se<sub>3</sub>. (c) Texture coefficients of diffraction peaks based on XRD patterns.

It is well known that film orientation is crucial for Sb<sub>2</sub>Se<sub>3</sub> thin film solar cells. To quantify the difference of preferential orientations between different Te-Sb<sub>2</sub>Se<sub>3</sub> thin films at different annealing temperatures, the texture coefficient (TC) of diffraction peaks was calculated using the following equation:

$$TC_{hkl} = \frac{I_{(hkl)}}{I_{0(hkl)}} / \left( \frac{1}{N} \sum_N \frac{I_{(hkl)}}{I_{0(hkl)}} \right), \quad (1)$$

where  $I_{(hkl)}$  is the measured diffraction peak intensity of (hkl) plane and  $I_{0(hkl)}$  is the intensity value in the standard XRD pattern.  $N$  is the total number of planes considered for the calculation. In general, a larger TC value implies a preferred orientation of grain in films [18]. As observed in Figure 2c,

the film annealed at 350 °C exhibited the strongest overall TC values for the (hk1) planes, further indicating the desired orientation for photovoltaic applications.

To better understand the mechanism of Te doping, the lattice parameters of Te-Sb<sub>2</sub>Se<sub>3</sub> thin films were calculated using JADE 6.0 software, as shown in Figure 3. Referring to the different annealing temperatures, the thin films were denoted as 325-film, 350-film, 375-film, and 400-film, respectively. Obviously, the lattice parameter *a* (or *b*) of Te-Sb<sub>2</sub>Se<sub>3</sub> thin films slightly increased, while the lattice parameter *c* slightly decreased when compared with pure Sb<sub>2</sub>Se<sub>3</sub> [34]. It suggests that the lattice parameter along the directions that the (Sb<sub>4</sub>Se<sub>6</sub>)<sub>n</sub> ribbons were held together through weak van der Waals forces [6], i.e., the [100] and [010] axes increased remarkably. For an orthorhombic crystal, it is well known that the relationship between interplanar spacing (*d*<sub>hkl</sub>) and lattice constants (*a*, *b*, *c*) can be expressed as follows [34]:

$$d_{hkl} = \frac{1}{\left[\left(\frac{h}{a}\right)^2 + \left(\frac{k}{b}\right)^2 + \left(\frac{l}{c}\right)^2\right]^{0.5}}, \quad (2)$$

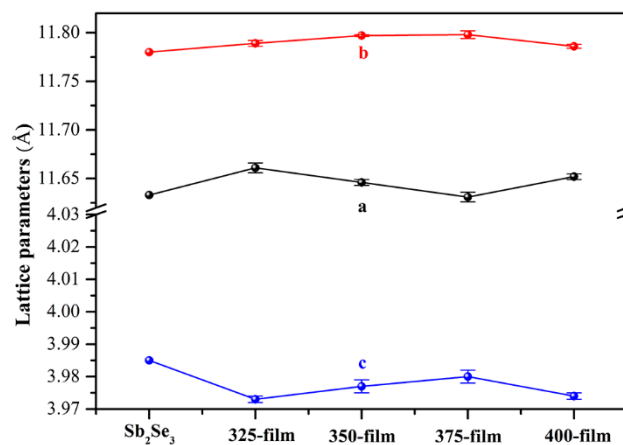


**Figure 3.** The lattice parameters of Te-Sb<sub>2</sub>Se<sub>3</sub> thin films at different annealing temperatures and pure Sb<sub>2</sub>Se<sub>3</sub>.

As a result, increased lattice parameters resulted in broadened interplanar spacing and the (230) diffraction peak shifted toward a lower angle (Figure 2b). Moreover, compared with the intrinsic p-type nature of pure Sb<sub>2</sub>Se<sub>3</sub> thin film, the conductivity type of Te-Sb<sub>2</sub>Se<sub>3</sub> thin films was n-type, as verified by the PN tester. Considering the larger lattice parameters and the n-type doping behavior, we thus further believe that Te element was mainly located in the gap between the (Sb<sub>4</sub>Se<sub>6</sub>)<sub>n</sub> ribbons and was a donor in the Sb<sub>2</sub>Se<sub>3</sub> film. Such a phenomenon has been frequently found for Cd and Na doping in Sb<sub>2</sub>Se<sub>3</sub> as well [6,25].

Figure 4 displays scanning electron microscopy (SEM) images of the Te-Sb<sub>2</sub>Se<sub>3</sub> thin films with different annealing temperatures. For 325 °C-annealed thin film, small crystal grains were apparent (Figure 4a). In contrast, the grain size increased in the 350 °C-annealed thin film, accompanied by many round grains (red circles, Figure 4b), and thus the intensities of diffraction peaks (211) and (221) were higher (Figure 2a). Notably, the film annealed at 350 °C was compact and free of cracks. When the annealing temperature increased to 375 °C, the morphology of film was considerably different from the 350 °C-annealed thin film; a large number of rod grains (red ellipses, Figure 4c) appeared along with large melted/softened areas. The intensity of diffraction peak (120) was enhanced; however, the (211) and (221) orientations were reduced (Figure 2a). Meanwhile, the 375 °C crystalline film showed loose grain boundaries due to thermal etching, as already observed in similar materials [26]. By further increasing the temperature to 400 °C, the film significantly deteriorated, leading to the formation of apparent holes (yellow circles, Figure 4d) and sparse surfaces due to excessive thermal etching.

Therefore, the annealing temperature plays a crucial role in achieving high-quality Te-Sb<sub>2</sub>Se<sub>3</sub> film. As seen in Figure 4e-h, a good interface quality without cracks was generally observed.

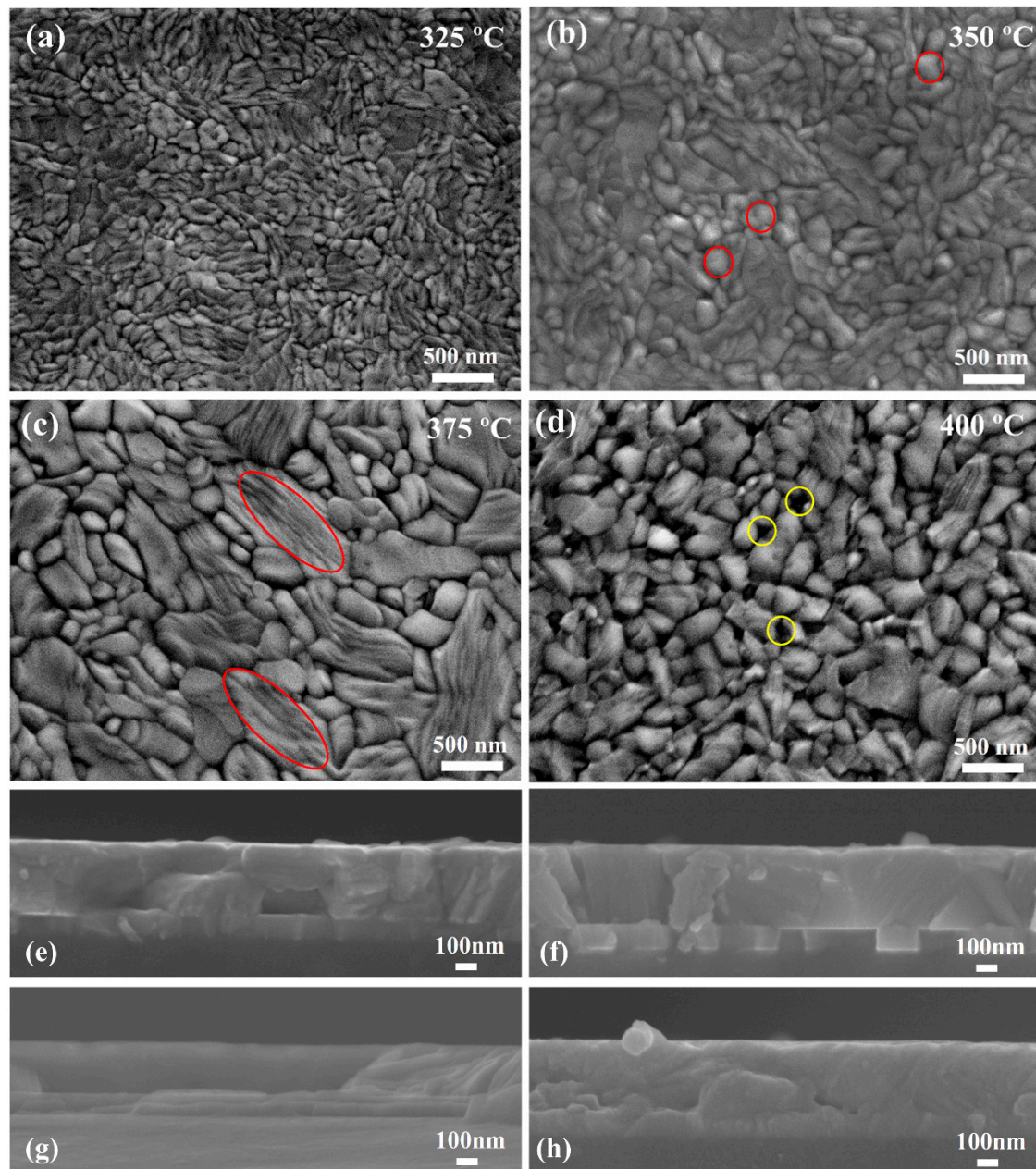


**Figure 4.** Top-views and cross-section SEM images of the Te-Sb<sub>2</sub>Se<sub>3</sub> thin films annealed at temperatures of (a,e) 325, (b,f) 350, (c,g) 375, and (d,h) 400 °C.

### 3.3. Optical Properties of Te-Sb<sub>2</sub>Se<sub>3</sub> Thin Films

In order to further investigate the optical properties of the Te-Sb<sub>2</sub>Se<sub>3</sub> thin films, an UV/Vis/NIR spectrophotometer was used to measure the reflection and transmission at room temperature in a wavelength range of 500–1500 nm with glass as the substrate. As observed in Figure 5a, the reflectance of the as-deposited thin film was much lower than that of the crystalline thin films in the short wavelength region, mainly due to its density-dependent lower refractive index as well as its disorder. Moreover, the red-shift of the short wavelength cut-off edge from 640 nm for the as-deposited thin film to around 876 nm for the crystalline thin film was evident, resulting in the evolution of the band gap.



To further evaluate the effect of Te doping on the band structure, the band gap width ( $E_g$ ) of the thin films was calculated using the following formulas:

$$\alpha = \frac{1}{d} \ln\left(\frac{1-R(\lambda)}{T(\lambda)}\right), \quad (3)$$

$$\alpha h\nu = B(h\nu - E_g)^r, \quad (4)$$

where  $\alpha$  is the absorption coefficient;  $d$  is thickness of thin film (350 nm); and  $R$  and  $T$  represent the reflectance and transmittance, respectively [35]. Equation (4) is a classical Tauc relationship, where  $B$  is a constant;  $\nu$  is the photo frequency;  $h$  is the Planck's constant; and  $r = 2$  for an indirect band gap semiconductor and  $r = 0.5$  for a direct band gap semiconductor [4]. As shown in Figure 5c, the as-deposited thin film possessed a direct band gap of 1.65 eV; the value remarkably decreased to around 1.27 eV after annealing due to the change in atomic arrangement from disorder to order. A slight increase in the band gap width compared with pure  $\text{Sb}_2\text{Se}_3$  thin film (1.15 eV) [36] was observed after Te doping, which is ascribed to the combination of the Burstein–Moss shift and the renormalization effect, existing in the narrow band gap semiconductor with a certain doping level [37,38]. On the whole, the band gap of the  $\text{Te-Sb}_2\text{Se}_3$  thin films is still suitable for efficiently harvesting visible light.

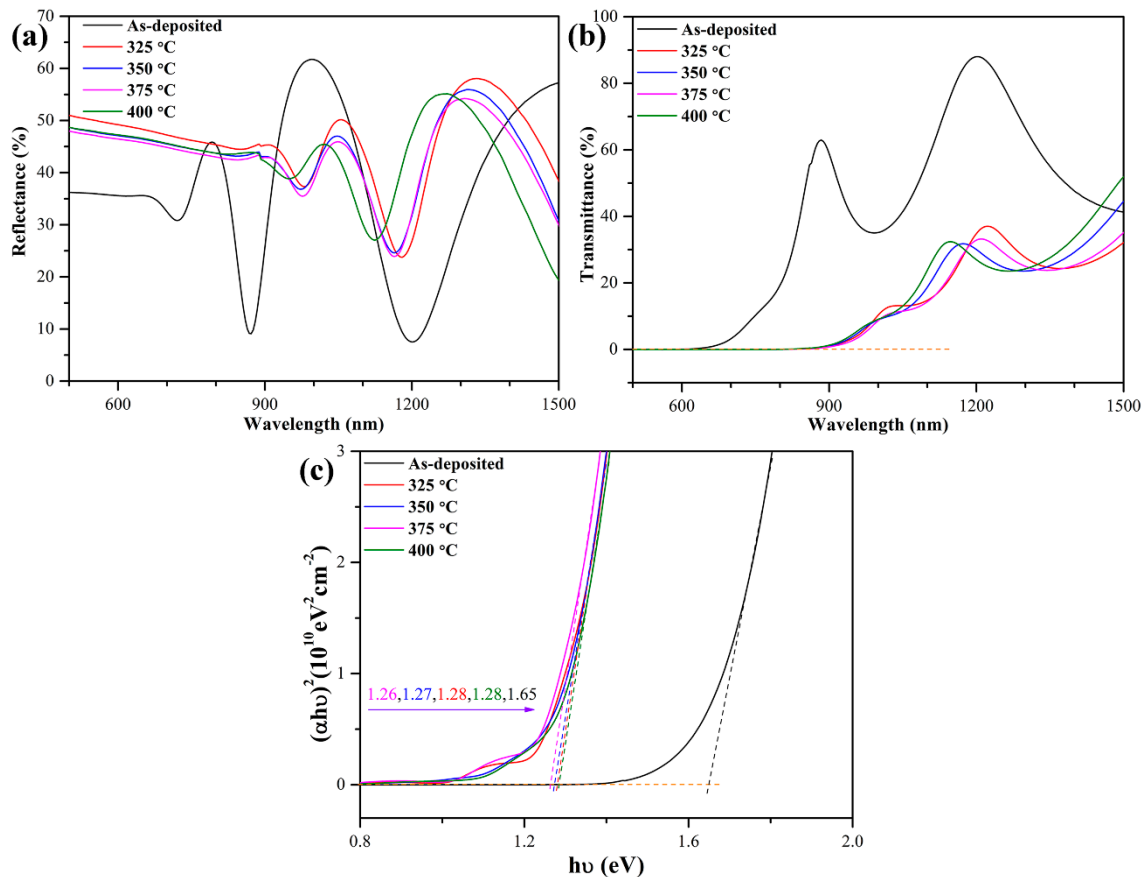


**Figure 5.** Optical characterizations of  $\text{Te-Sb}_2\text{Se}_3$  thin films at different annealing temperatures. (a) Reflection spectra, (b) Transmission spectra, and (c) Plot of  $(\alpha h\nu)^2$  vs.  $h\nu$  for obtaining the direct band gap.

### 3.4. Photoelectric Performances of $\text{Te-Sb}_2\text{Se}_3$ Thin Films

To evaluate the PEC performance of the  $\text{Te-Sb}_2\text{Se}_3$  films annealed at different temperatures, photo-electro-chemical measurements were performed under chopped light with an intensity of  $10.5 \text{ mW/cm}^2$ . As can be observed in Figure 6, all  $\text{Te-Sb}_2\text{Se}_3$  films showed anodic photocurrents,

and their photocurrent density increased with the positive bias, indicating that Te-Sb<sub>2</sub>Se<sub>3</sub> films are n-type semiconductors, which is in agreement with the result obtained from the PN tester. There was no apparent variation in the photocurrent response at the potential between 0.5 and 0.75 V. It is well known that Sb<sub>2</sub>Se<sub>3</sub> apparently shows direction-dependent bonding characteristics. The carrier transport in the [001] direction occurred much easily than in the [221] direction, in which the (Sb<sub>4</sub>Se<sub>6</sub>)<sub>n</sub> ribbons were tilted at a smaller angle with the substrate [8]. Compared with the 350 °C-annealed Te-Sb<sub>2</sub>Se<sub>3</sub> film, the reduced intensity of the diffraction peaks (221) and (211) for other crystalline films (Figure 2a) implies that they grew with improved preference along the [001] direction (c-axis), resulting in higher photocurrent density. In addition, the photocurrent density obviously depends on the quality of the films. As a result, a maximum photocurrent density of 1.91 mA/cm<sup>2</sup> at around 1.4 V was obtained for the film annealed at 325 °C. On the contrary, the lowest response of 0.23 mA/cm<sup>2</sup> was observable for 350 °C-annealed film. Moreover, Te was shown to significantly reduce deep level defects, due to the improved conductivity and reduced recombination, leading to a longer carrier lifetime [23]. As a result, the Te-Sb<sub>2</sub>Se<sub>3</sub> film was shown to possess much better photoelectric properties than pure Sb<sub>2</sub>Se<sub>3</sub> film.

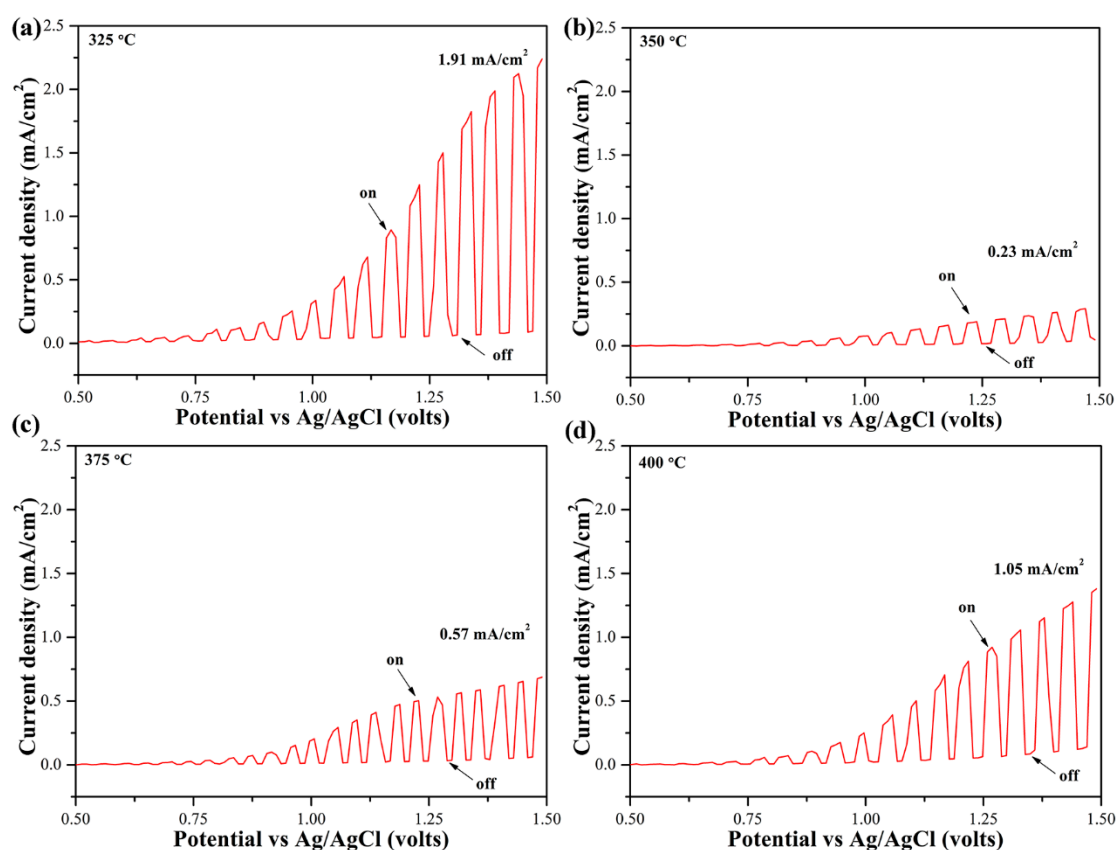


**Figure 6.** Photocurrent-potential response curves of Te-Sb<sub>2</sub>Se<sub>3</sub> films with different annealing temperatures: (a) 325, (b) 350, (c) 375, and (d) 400 °C.

The cyclic photoresponse of the Te-Sb<sub>2</sub>Se<sub>3</sub> films was also characterized, as shown in Figure 7a. Clearly, the photocurrent density of the Te-Sb<sub>2</sub>Se<sub>3</sub> film annealed at 325 °C showed a slight decline during several cycles, while the 350 °C-annealed Te-Sb<sub>2</sub>Se<sub>3</sub> film was stabilized almost at its original level. This is attributed to the low-density morphology that makes the 325 °C film more susceptible to oxydo-reduction. The response ( $\tau_{on}$ ) and recovery ( $\tau_{off}$ ) times are two important parameters that can be used to assess the speed of the on/off switching, which is defined as the time between 10% and 90% values of the maximum current. As observed in Figure 7b and c, the 350 °C film shows a shorter response time of 0.01 s and recovery time of 0.015 s, which is ascribed to higher crystal quality, preferential orientation, and the grain size [16]. Furthermore, the discrepancy in response/recovery times may result

from the traps and other defects [39], leading to increased recombination of photogenerated carriers in the 350 °C film. Notably, the response time of the Te-Sb<sub>2</sub>Se<sub>3</sub> film was shorter than that mentioned in many previous literatures [39,40], suggesting its high application potential as excellent photodetectors.

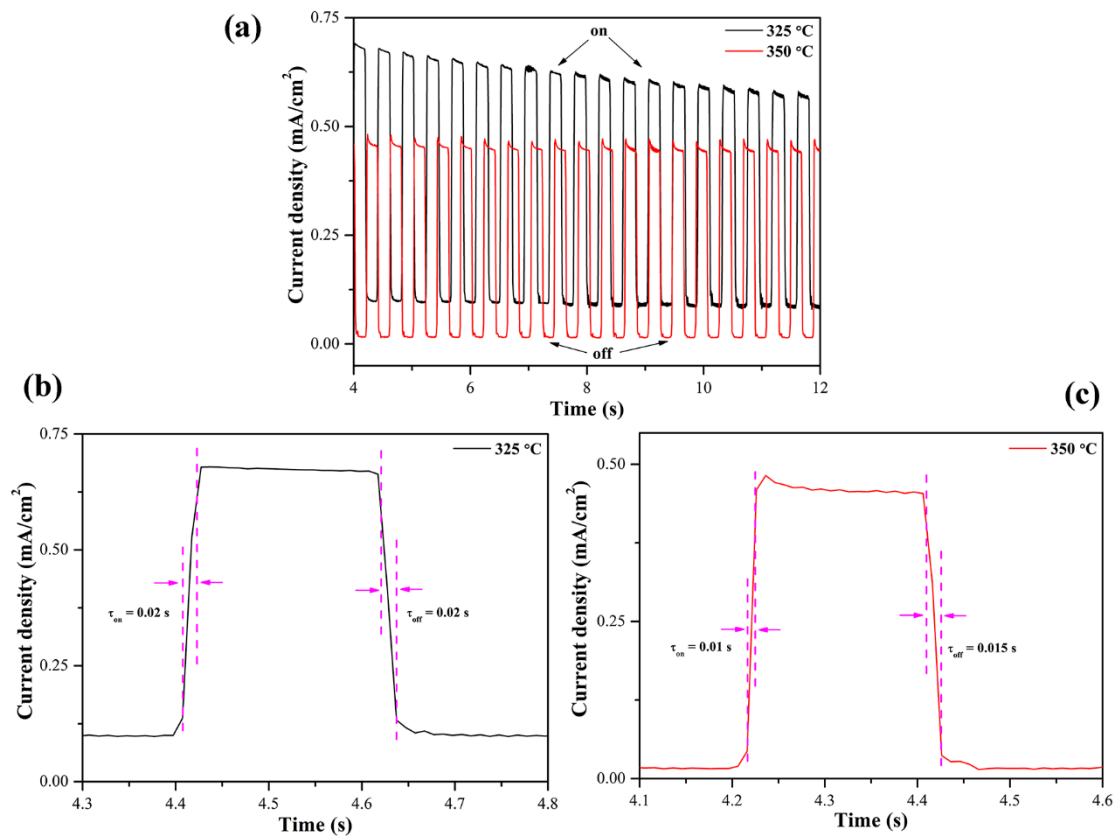


**Figure 7.** (a) Time-resolved PEC photoresponse of Te-Sb<sub>2</sub>Se<sub>3</sub> films annealed at 325 and 350 °C. (b) and (c) show the response and recovery times, respectively.

#### 4. Conclusions

N-type Sb<sub>2</sub>Se<sub>3</sub> was obtained through Te doping, and high-quality thin films were prepared by using magnetron sputtering. It was found that post-deposition annealing has a crucial influence on the properties of the films. Different investigations showed that Te atoms are inserted into the spacing of (Sb<sub>4</sub>Se<sub>6</sub>)<sub>n</sub> ribbons as donors based on increased lattice parameters. All of the films maintained a narrow band gap of approximately 1.27 eV, ideal for harvesting the solar energy. The photoelectric performance of the films was also found to be highly dependent on the annealing temperatures, and the film annealed at 325 °C realized a maximum photocurrent density of 1.91 mA/cm<sup>2</sup> with a light intensity of 10.5 mW/cm<sup>2</sup> at a bias of 1.4 V. The fast response and strong photocurrent density give these films the potential to be used as photodetectors as well as for photovoltaic application.

**Author Contributions:** Conceptualization, X.Z.; Data curation, H.M.; Formal analysis, D.R., X.L., S.C., Z.Z., G.L. and H.M.; Investigation, D.R.; Methodology, M.C.; Project administration, X.Z.; Supervision, X.Z.; Validation, X.Z.; Visualization, X.Q. and X.F.; Writing—original draft, D.R.; Writing—review & editing, X.Z. All authors have read and agreed to the published version of the manuscript.

**Funding:** We gratefully acknowledge the China Scholarship Council for providing a PhD scholarship (201804910786). This work was also supported by Key Project of Department of Education of Guangdong Province (No. 2018KZDXM059) China, Science and Technology plan project of Shenzhen (JCYJ20190808153409238) China, Natural Science Foundation of Guangdong Province (2020A1515010805) China.

**Acknowledgments:** We thank Francis Gouttefangeas and Loic Joanny for their contributions to the electron microscopy observations. We also thank the assistance on XRD data received from François Cheviré and Franck Tessier.

**Conflicts of Interest:** The authors declare no conflict of interest.

## References

1. Photovoltaics Report. 2020. Available online: <https://www.ise.fraunhofer.de/content/dam/ise/de/documents/publications/studies/Photovoltaics-Report.pdf> (accessed on 23 April 2020).
2. Lei, H.; Chen, J.; Tan, Z.; Fang, G. Review of recent progress in antimony chalcogenide-based solar cells: Materials and devices. *Sol. RRL* **2019**, *3*, 1900026. [[CrossRef](#)]
3. Zhang, L.; Jiang, C.; Wu, C.; Ju, H.; Jiang, G.; Liu, W.; Zhu, C.; Chen, T. V<sub>2</sub>O<sub>5</sub> as hole transporting material for efficient all inorganic Sb<sub>2</sub>S<sub>3</sub> solar cells. *ACS Appl. Mater. Interfaces* **2018**, *10*, 27098–27105. [[CrossRef](#)] [[PubMed](#)]
4. Luo, J.; Xiong, W.; Liang, G.; Liu, Y.; Yang, H.; Zheng, Z.; Zhang, X.; Fan, P.; Chen, S. Fabrication of Sb<sub>2</sub>Se<sub>3</sub> thin films by magnetron sputtering and post-sulfurization/selenization for substrate structured solar cells. *J. Alloys Compd.* **2020**, *826*, 154235. [[CrossRef](#)]
5. Liu, X.; Chen, J.; Luo, M.; Leng, M.; Xia, Z.; Zhou, Y.; Qin, S.; Xue, D.J.; Lv, L.; Huang, H.; et al. Thermal evaporation and characterization of Sb<sub>2</sub>Se<sub>3</sub> thin film for substrate Sb<sub>2</sub>Se<sub>3</sub>/CdS solar cells. *ACS Appl. Mater. Interfaces* **2014**, *6*, 10687–10695. [[CrossRef](#)] [[PubMed](#)]
6. Zhou, Y.; Li, Y.; Luo, J.; Li, D.; Liu, X.; Chen, C.; Song, H.; Ma, J.; Xue, D.-J.; Yang, B.; et al. Buried homojunction in CdS/Sb<sub>2</sub>Se<sub>3</sub> thin film photovoltaics generated by interfacial diffusion. *Appl. Phys. Lett.* **2017**, *111*, 013901. [[CrossRef](#)]
7. Ma, C.; Guo, H.; Wang, X.; Chen, Z.; Cang, Q.; Jia, X.; Li, Y.; Yuan, N.; Ding, J. Fabrication of Sb<sub>2</sub>Se<sub>3</sub> thin film solar cells by co-sputtering of Sb<sub>2</sub>Se<sub>3</sub> and Se targets. *Sol. Energy* **2019**, *193*, 275–282. [[CrossRef](#)]
8. Li, Z.; Liang, X.; Li, G.; Liu, H.; Zhang, H.; Guo, J.; Chen, J.; Shen, K.; San, X.; Yu, W.; et al. 9.2%-efficient core-shell structured antimony selenide nanorod array solar cells. *Nat. Commun.* **2019**, *10*, 1–9. [[CrossRef](#)]
9. Tang, R.; Chen, X.; Luo, Y.; Chen, Z.; Liu, Y.; Li, Y.; Su, Z.; Zhang, X.; Fan, P.; Liang, G. Controlled sputtering pressure on high-quality Sb<sub>2</sub>Se<sub>3</sub> thin film for substrate configured solar cells. *Nanomaterials* **2020**, *10*, 574. [[CrossRef](#)]
10. Chen, C.; Bobela, D.C.; Yang, Y.; Lu, S.; Zeng, K.; Ge, C.; Yang, B.; Gao, L.; Zhao, Y.; Beard, M.C.; et al. Characterization of basic physical properties of Sb<sub>2</sub>Se<sub>3</sub> and its relevance for photovoltaics. *Front. Optoelectron.* **2017**, *10*, 18–30. [[CrossRef](#)]
11. Ren, D.; Merdignac-Conanec, O.; Dorcet, V.; Cathelinaud, M.; Zheng, Z.; Ma, H.; Zhang, X. In situ synthesis and improved photoelectric performances of a Sb<sub>2</sub>Se<sub>3</sub>/β-In<sub>2</sub>Se<sub>3</sub> heterojunction composite with potential photocatalytic activity for methyl orange degradation. *Ceram. Int.* **2020**. [[CrossRef](#)]
12. Huang, M.; Xu, P.; Han, D.; Tang, J.; Chen, S. Complicated and unconventional defect properties of the quasi-one-dimensional photovoltaic semiconductor Sb<sub>2</sub>Se<sub>3</sub>. *ACS Appl. Mater. Interfaces* **2019**, *11*, 15564–15572. [[CrossRef](#)] [[PubMed](#)]
13. Tang, R.; Zheng, Z.H.; Su, Z.H.; Li, X.J.; Wei, Y.D.; Zhang, X.H.; Fu, Y.Q.; Luo, J.T.; Fan, P.; Liang, G.X. Highly efficient and stable planar heterojunction solar cell based on sputtered and post-selenized Sb<sub>2</sub>Se<sub>3</sub> thin film. *Nano Energy* **2019**, *64*, 103929. [[CrossRef](#)]
14. Liu, X.; Xiao, X.; Yang, Y.; Xue, D.-J.; Li, D.-B.; Chen, C.; Lu, S.; Gao, L.; He, Y.; Beard, M.C.; et al. Enhanced Sb<sub>2</sub>Se<sub>3</sub> solar cell performance through theory-guided defect control. *Prog. Photovolt. Res. Appl.* **2017**, *25*, 861–870. [[CrossRef](#)]
15. Tao, J.; Hu, X.; Guo, Y.; Hong, J.; Li, K.; Jiang, J.; Chen, S.; Jing, C.; Yue, F.; Yang, P.; et al. Solution-processed SnO<sub>2</sub> interfacial layer for highly efficient Sb<sub>2</sub>Se<sub>3</sub> thin film solar cells. *Nano Energy* **2019**, *60*, 802–809. [[CrossRef](#)]
16. Chen, S.; Qiao, X.; Zheng, Z.; Cathelinaud, M.; Ma, H.; Fan, X.; Zhang, X. Enhanced electrical conductivity and photoconductive properties of Sn-doped Sb<sub>2</sub>Se<sub>3</sub> crystals. *J. Mater. Chem. C* **2018**, *6*, 6465–6470. [[CrossRef](#)]
17. Zhou, Y.; Leng, M.; Xia, Z.; Zhong, J.; Song, H.; Liu, X.; Yang, B.; Zhang, J.; Chen, J.; Zhou, K.; et al. Solution-processed antimony selenide heterojunction solar cells. *Adv. Energy Mater.* **2014**, *4*, 1301846. [[CrossRef](#)]
18. Li, K.; Chen, C.; Lu, S.; Wang, C.; Wnag, S.; Lu, Y.; Tang, J. Orientation engineering in low-dimensional crystal-structural materials via seed screening. *Adv. Mater.* **2019**, *31*, 1903914. [[CrossRef](#)]
19. Yuan, C.; Zhang, L.; Liu, W.; Zhu, C. Rapid thermal process to fabricate Sb<sub>2</sub>Se<sub>3</sub> thin film for solar cell application. *Sol. Energy* **2016**, *137*, 256–260. [[CrossRef](#)]

20. Liang, G.-X.; Zheng, Z.-H.; Fan, P.; Luo, J.-T.; Hu, J.-G.; Zhang, X.-H.; Ma, H.-L.; Fan, B.; Luo, Z.-K.; Zhang, D.-P. Thermally induced structural evolution and performance of  $\text{Sb}_2\text{Se}_3$  films and nanorods prepared by an easy sputtering method. *Sol. Energy Mater. Sol. Cells* **2018**, *174*, 263–270. [[CrossRef](#)]
21. Luo, Y.-D.; Tang, R.; Chen, S.; Hu, J.-G.; Liu, Y.-K.; Li, Y.-F.; Liu, X.-S.; Zheng, Z.-H.; Su, Z.-H.; Ma, X.-F.; et al. An effective combination reaction involved with sputtered and selenized Sb precursors for efficient  $\text{Sb}_2\text{Se}_3$  thin film solar cells. *Chem. Eng. J.* **2020**, *393*, 124599. [[CrossRef](#)]
22. Liang, G.-X.; Luo, Y.-D.; Chen, S.; Tang, R.; Zheng, Z.-H.; Li, X.-J.; Liu, X.-S.; Liu, Y.-K.; Li, Y.-F.; Chen, X.-Y.; et al. Sputtered and selenized  $\text{Sb}_2\text{Se}_3$  thin-film solar cells with open-circuit voltage exceeding 500 mV. *Nano Energy* **2020**, *73*, 104806. [[CrossRef](#)]
23. Ma, Y.; Tang, B.; Lian, W.; Wu, C.; Wang, X.; Ju, H.; Zhu, C.; Fan, F.; Chen, T. Efficient Defect Passivation of  $\text{Sb}_2\text{Se}_3$  Film by Tellurium Doping for High Performance Solar Cells. *J. Mater. Chem. A* **2020**, *8*, 6510–6516. [[CrossRef](#)]
24. Said, S.M.; Bashir, M.B.A.; Sabri, M.F.M.; Miyazaki, Y.; Shnawah, D.A.A.; Hakeem, A.S.; Shimada, M.; Bakare, A.I.; Ghazali, N.N.N.; Elsheikh, M.H. Enhancement of thermoelectric behavior of  $\text{La}_{0.5}\text{Co}_4\text{Sb}_{12-x}\text{Te}_x$  skutterudite materials. *Metall. Mater. Trans. A* **2017**, *48*, 3073–3081. [[CrossRef](#)]
25. Li, Y.; Zhou, Y.; Luo, J.; Chen, W.; Yang, B.; Wen, X.; Lu, S.; Chen, C.; Zeng, K.; Song, H.; et al. The effect of sodium on antimony selenide thin film solar cells. *RSC Adv.* **2016**, *6*, 87288–87293. [[CrossRef](#)]
26. Chen, S.; Zheng, Z.; Cathelinaud, M.; Ma, H.; Qiao, X.; Su, Z.; Fan, P.; Liang, G.; Fan, X.; Zhang, X. Magnetron sputtered  $\text{Sb}_2\text{Se}_3$ -based thin films towards high performance quasi-homojunction thin film solar cells. *Sol. Energy Mater. Sol. Cells* **2019**, *203*, 110154. [[CrossRef](#)]
27. Ren, D.; Chen, S.; Cathelinaud, M.; Liang, G.-X.; Ma, H.; Zhang, X. Fundamental physical characterization of  $\text{Sb}_2\text{Se}_3$ -based quasi-homojunction thin film solar cells. *ACS Appl. Mater. Interfaces* **2020**, *12*, 30572–30583. [[CrossRef](#)]
28. Ren, D.; Zheng, Z.; Wei, M.; Zhang, P.; Cathelinaud, M.; Ma, H.; Zhang, X. Synthesis, structure and photoelectric properties of selenide composites with in situ constructed  $\text{Sb}_2\text{Se}_3/\text{NaSbSe}_2$  heterojunction. *J. Eur. Ceram. Soc.* **2020**, *40*, 4517–4526. [[CrossRef](#)]
29. Zhou, Y.; Wang, L.; Chen, S.; Qin, S.; Liu, X.; Chen, J.; Xue, D.J.; Luo, M.; Cao, Y.; Cheng, Y.; et al. Thin-film  $\text{Sb}_2\text{Se}_3$  photovoltaics with oriented one-dimensional ribbons and benign grain boundaries. *Nat. Photonics* **2015**, *9*, 409–415. [[CrossRef](#)]
30. Liang, G.; Chen, X.; Tang, R.; Liu, Y.; Li, Y.; Luo, P.; Su, Z.; Zhang, X.; Fan, P.; Chen, S. Spark plasma sintering of  $\text{Sb}_2\text{Se}_3$  sputtering target towards highly efficient thin film solar cells. *Sol. Energy Mater. Sol. Cells* **2020**, *211*, 110530. [[CrossRef](#)]
31. Ren, D.; Deng, Q.; Wang, J.; Li, Y.; Li, M.; Ran, S.; Du, S.; Huang, Q. Densification and mechanical properties of pulsed electric current sintered  $\text{B}_4\text{C}$  with in situ synthesized  $\text{Al}_3\text{BC}$  obtained by the molten-salt method. *J. Eur. Ceram. Soc.* **2017**, *37*, 4524–4531. [[CrossRef](#)]
32. Ren, D.; Deng, Q.; Wang, J.; Yang, J.; Li, Y.; Shao, J.; Li, M.; Zhou, J.; Ran, S.; Du, S.; et al. Synthesis and properties of conductive  $\text{B}_4\text{C}$  ceramic composites with  $\text{TiB}_2$  grain network. *J. Am. Ceram. Soc.* **2018**, *101*, 3780–3786. [[CrossRef](#)]
33. Wang, J.; Ren, D.; Chen, L.; Man, G.; Zhang, H.; Zhang, H.; Luo, L.; Li, W.; Pan, Y.; Gao, P.; et al. Initial investigation of  $\text{B}_4\text{C}$ - $\text{TiB}_2$  composites as neutron absorption material for nuclear reactors. *J. Nucl. Mater.* **2020**, *539*, 152275. [[CrossRef](#)]
34. Tian, Y.; Sun, Z.; Zhao, Y.; Zhang, Y.; Tan, T.; Yin, F. Facile spray drying approach to synthesize  $\text{Sb}_2\text{Se}_3/\text{rGO}$  composite anode for lithium-ion battery. *J. Nanoparticle Res.* **2019**, *21*, 15. [[CrossRef](#)]
35. Kobayashi, T.; Kumazawa, T.; Kao, Z.J.L.; Nakada, T.  $\text{Cu}(\text{In,Ga})\text{Se}_2$  thin film solar cells with a combined ALD-Zn(O,S) buffer and MOCVD-ZnO:B window layers. *Sol. Energy Mater. Sol. Cells* **2013**, *119*, 129–133. [[CrossRef](#)]
36. Chen, C.; Li, W.; Zhou, Y.; Chen, C.; Luo, M.; Liu, X.; Zeng, K.; Yang, B.; Zhang, C.; Han, J.; et al. Optical properties of amorphous and polycrystalline  $\text{Sb}_2\text{Se}_3$  thin films prepared by thermal evaporation. *Appl. Phys. Lett.* **2015**, *107*, 043905. [[CrossRef](#)]
37. Walsh, A.; Da Silva, J.L.F.; Wei, S.H. Origins of band-gap renormalization in degenerately doped semiconductors. *Phys. Rev. B Condens. Matter Mater. Phys.* **2008**, *78*, 075211. [[CrossRef](#)]
38. Gibbs, Z.M.; LaLonde, A.; Snyder, G.J. Optical band gap and the Burstein-Moss effect in iodine doped PbTe using diffuse reflectance infrared Fourier transform spectroscopy. *New J. Phys.* **2013**, *15*, 075020. [[CrossRef](#)]

39. Liu, Y.-Q.; Zhang, M.; Wang, F.-X.; Pan, G.-B. Facile microwave-assisted synthesis of uniform  $\text{Sb}_2\text{Se}_3$  nanowires for high performance photodetectors. *J. Mater. Chem. C* **2014**, *2*, 240–244. [[CrossRef](#)]
40. Zhai, T.; Ye, M.; Li, L.; Fang, X.; Liao, M.; Li, Y.; Koide, Y.; Bando, Y.; Golberg, D. Single-crystalline  $\text{Sb}_2\text{Se}_3$  nanowires for high-performance field emitters and photodetectors. *Adv. Mater.* **2010**, *22*, 4530–4533. [[CrossRef](#)]



© 2020 by the authors. Licensee MDPI, Basel, Switzerland. This article is an open access article distributed under the terms and conditions of the Creative Commons Attribution (CC BY) license (<http://creativecommons.org/licenses/by/4.0/>).